

In-plane epitaxy strain tuning intralayer and interlayer magnetic couplings in CrSe₂ and CrTe₂ mono- and bi-layers

Linlu Wu^{1, †}, Linwei Zhou^{1, †}, Xieyu Zhou¹, Cong Wang^{1, *} and Wei Ji^{1, *}

¹*Beijing Key Laboratory of Optoelectronic Functional Materials & Micro-Nano Devices,
Department of Physics, Renmin University of China, Beijing 100872, P.R. China*

Corresponding authors: C.W. (email: wcphys@ruc.edu.cn), W.J. (email: wji@ruc.edu.cn)

† These authors contributed equally to this work.

Mismatched lattice-constants at a van-der-Waals epitaxy interface often introduce in-plane strains to the lattice of the epitaxial layer, termed epitaxy-strain, where the strains do not follow the intra-layer Poisson's relation. Here, we presented the magnetic phase diagrams of the CrSe₂ and CrTe₂ mono- and bi-layers under epitaxy-strain up to 8 %, as predicted using density-functional-theory calculations. They show that the in-plane epitaxy-strain manipulates either the intra- or inter-layer magnetism of them. The in-plane strain varies the interlayer distance, defined using an inter-layer Poisson's ratio, which governs the inter-layer magnetism in two opposite ways depending on the in-plane magnetism. The tunability of the intra-layer magnetism is a result of competing intra-layer Cr-Cr super-exchange interactions. A graphene substrate was introduced to examine the validity of our diagrams in practice. Our work also gives a tentative explanation on the controversially reported magnetizations in CrSe₂ and CrTe₂ epitaxial mono- or bi-layers under epitaxy-strains.

Magnetism in two dimensional (2D) van der Waals (vdW) materials has received extensive attention in recent years. Strain engineering appears an effective route to manipulate magnetism in 2D materials, which was experimentally realized through, e.g., hydrostatic pressure for CrI_3 [1-3] and uniaxial strain for Fe_3GeTe_2 [4] recently. In a more ideal case, theoretical calculations showed that a uniformly in-plane biaxial strain could tune the magnetic ground states of CrSe_2 and CrTe_2 monolayers, which is yet to be experimentally verified [5]. In these studies, strain induced lattice variations are either uniform (biaxial strain or hydrostatic pressure) or coupled with the Poisson's ratio of the material. Thus, few of previous studies have dealt with the case where in-plane strains are independently applied along with the two lattice vectors of a 2D magnet, which are usually occurred in epitaxy growth of layered materials.

Epitaxy of heterostructures usually introduces lateral interfacial strains because of lattice mismatch, which is a long-lasting way to maintain in-plane strain to the adlayers and is thus termed epitaxy strain [6-8]. VdW epitaxy refers to growth of 2D layers through vdW interactions on a dangling-bond-free substrate [9, 10]. Magnetic 2D layers in vdW heterostructures show a strong ability to bear with large lattice mismatches and thus significant in-plane strains [11-13]. A recent illustration of this ability lies in epitaxy of monolayer CrTe_2 on graphene where a 7 % compressive and a 4 % tensile epitaxy strain were applied along the two lattice vectors, in which a zig-zag anti-ferromagnetic (AFM) order was observed [12]. This is not an isolated example that a 6 % epitaxy tensile strain was applied in the both lattice directions of a CrSe_2 monolayer through epitaxy growth on WSe_2 where a weak ferromagnetic (FM) state was reported [13]. In comparison with the ABAB order predicted in the free-standing CrSe_2 monolayer, it implies a potential ability of epitaxy strain to tune in-plane magnetism of 2D magnets, which is yet to be fully unveiled. In-plane magnetism aside, an interesting question is subsequently arisen that whether in-plane strains could change inter-layer spin-exchange couplings.

In this work, we comprehensively considered the roles of epitaxy strain in tuning intra- and inter-plane magnetic couplings in CrSe_2 and CrTe_2 mono- and bi-layers using density functional theory calculations. The predicted magnetic phase diagram of the CrSe_2 (CrTe_2) monolayer shows that its intralayer magnetic ground-state is tunable among FM and three AFM orders within a 2.5 % (4.5 %) in-plane strain. This tunability is primarily realized by

changing Cr-Se-Cr (Cr-Te-Cr) angles and thus the strength and type of Se (Te) mediated super-exchange interactions between adjacent Cr atoms. Moreover, the varying in-plane strain also affects interlayer Se-Se or Te-Te distances and thus changes the interlayer magnetism between ferromagnetic (FM) and AFM in two different manners [14]. A CrTe₂ (1L)/Graphene (2L) heterostructure model, recently prepared in an epitaxy experiment [12], was used to verify the reliability and feasibility of the phase diagrams.

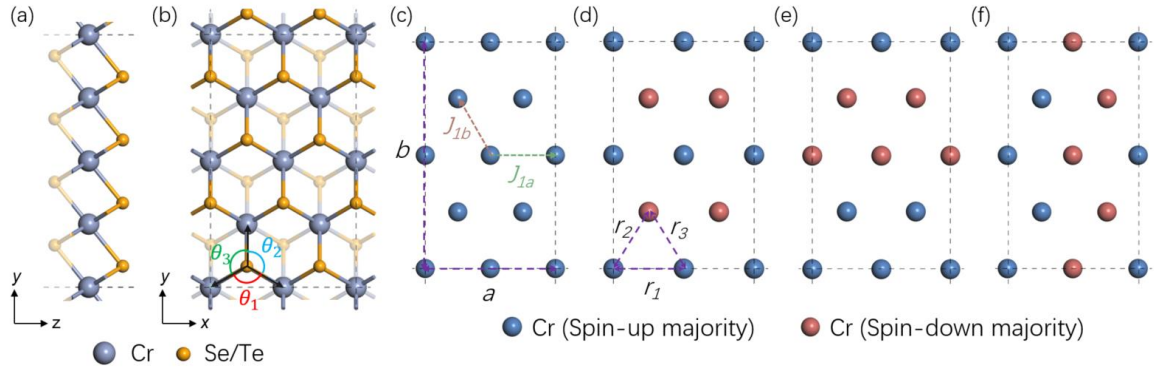


Figure 1. Schematic models and magnetic configurations of monolayer CrX₂. (a) and (b) Side and top views of monolayer 1T-CrX₂. The orange and grey balls represent top (solid) and bottom (semitransparent) layer Se (Te) and Cr atoms, respectively. Three colored arcs denote three Cr-Se-Cr (Cr-Te-Cr) angles θ_1 , θ_2 and θ_3 , respectively. Grey dash rectangles label the $2 \times 2\sqrt{3}$ supercell used for considering four magnetic configurations in (c)-(f). The dark blue (red) balls indicate Cr atoms where spin-up (down) is the majority spin-component. Lattice constants a and b are labeled using two purple dash lines in (c). Green and brown dashed arrows in (c) denote intralayer spin-exchange parameters J_{1a} and J_{1b} (nearly) in the a and b directions between the nearest Cr sites, respectively. Distances r_1 , r_2 and r_3 represent the nearest Cr-Cr distances in three lattice directions.

Both freestanding 1T-CrSe₂ and -CrTe₂ monolayers take a hexagonal crystal structure with the $P-3M1$ space group (Fig. 1a and 1b) in their paramagnetic states. A $2 \times 2\sqrt{3}$ rectangular supercell was used for considering four magnetic, i.e. FM (Fig. 1c), ABAB (Fig. 1d) and AABB (Fig. 1e) striped AFM (sAFM) and zigzag (ZZ, Fig. 1f) AFM, configurations in our calculations. Configuration sAFM-ABAB (ZZ-AFM) is the most two energetically favored configuration among all those considered ones of the CrSe₂ (CrTe₂) monolayer (see Table S1 for more details). The easy axis of CrSe₂ (CrTe₂) is oriented in the y - z plane and is 60° (100°) off the z axis (Fig. S1). Here, we employed the CrSe₂ monolayer as a prototype for discussion. Its fully relaxed FM structure (Fig. 1c), shows the lattice constants $a=6.84 \text{ \AA}$ and $b=11.84 \text{ \AA}$, the nearest Cr-Cr distance $r_1=r_2=r_3=3.42 \text{ \AA}$ and

the corresponding Cr-Se-Cr angle $\theta_1=\theta_2=\theta_3= 84.6^\circ$, exhibiting a C_3 rotational symmetry, which was chosen to be the non-strained structure for further comparison.

The C_3 symmetry, however, breaks in those three AFM configurations. Introduction of AFM spin-exchange coupling shortens r_2 and r_3 to 3.32 Å but elongates r_1 to 3.50 Å. The values of those angles split in accordance with the changes of Cr-Cr distances that θ_2 and θ_3 decrease to 81.7° and θ_1 increases to 86.8° . The lattice degeneracy further breaks in the ZZ configuration, which is the predicted groundstate for the CrTe₂ monolayer. In particular, the two AFM coupled distances r_1 and r_3 split into 3.59 and 3.57 Å, respectively, while the FM coupled distance reminds its FM configuration value of 3.66 Å. All associated angles decrease from $84.2 \pm 0.1^\circ$ to $\theta_1= 82.1^\circ$, $\theta_2= 81.7^\circ$ and $\theta_3=83.9^\circ$. These results indicate that magnetic configurations in the CrSe₂ (CrTe₂) monolayer is tightly coupled with their geometric structures, i.e. lattice constants, r_1 to r_3 and θ_1 to θ_3 . In light of this, it deserves a closer examination that the influence of geometric structures on magnetic orders in the both monolayers.

Figure 2a plots a magnetic phase diagram of the CrSe₂ monolayer as a function of lattice constants a and b . Tensile and compressive strains up to 8% were applied to the fully relaxed FM structure, i.e. $a=6.84$ Å and $b=11.84$ Å. While the FM configuration favors in expanded lattice constants, compression in the a (b) directions changes to the groundstate to the ZZ (ABAB) configuration. The AABB state appears to be the most stable in a very narrow window between the FM and ABAB phases. The phase diagram of CrTe₂ (Fig. 2b) shows a similar feature, but with much pronounced AABB region.

In the CrSe₂ (CrTe₂) monolayer, Se (Te) mediated Cr-Cr super-exchange interactions dominate its intralayer magnetism, which highly depends on the Cr-Se(Te)-Cr angle [15]. We thus defined spin-exchange parameters J_{1a} and J_{1b} along the two lattice directions (Fig. 1b) to explore the roles of varying in-plane epitaxy strain in changing θ_1 (Fig. 2c), θ_2 (Fig. 2e), J_{1a} (Fig. 2d) and J_{1b} (Fig. 2f) in the CrSe₂ monolayer as a prototype. Lattice constant a directly affects angle θ_1 and spin-exchange parameter J_{1a} , consequently the in-plane magnetic configuration. As shown in Fig. 2c-2f, in the FM region, angles θ_1 and θ_2 are very close to 90° and J_{1a} and J_{1b} are both negative in sign, which favors the Cr-Cr FM super-exchange. Angle θ_1 is nearly independent of lattice parameter b and gradually decreases with shrinking a values, i.e. from 90° at $a=7.30$ Å to 76° at $a=6.29$ Å with fixed $b=11.84$ Å

(the strain-free constant b value, Fig. 2c), which disfavors the Se mediated Cr-Cr FM super-exchange along the a direction. As a consequence, J_{1a} reverses its sign from negative to positive at, e.g. $a=7.04$ Å (~ 2.9 % tensile strain) with fixed $b=11.84$ Å, as marked using the purple dot in Fig. 2d, suggesting an FM to AFM transition. The sign reversal is the primary origin of the FM to ZZ-AFM transition.

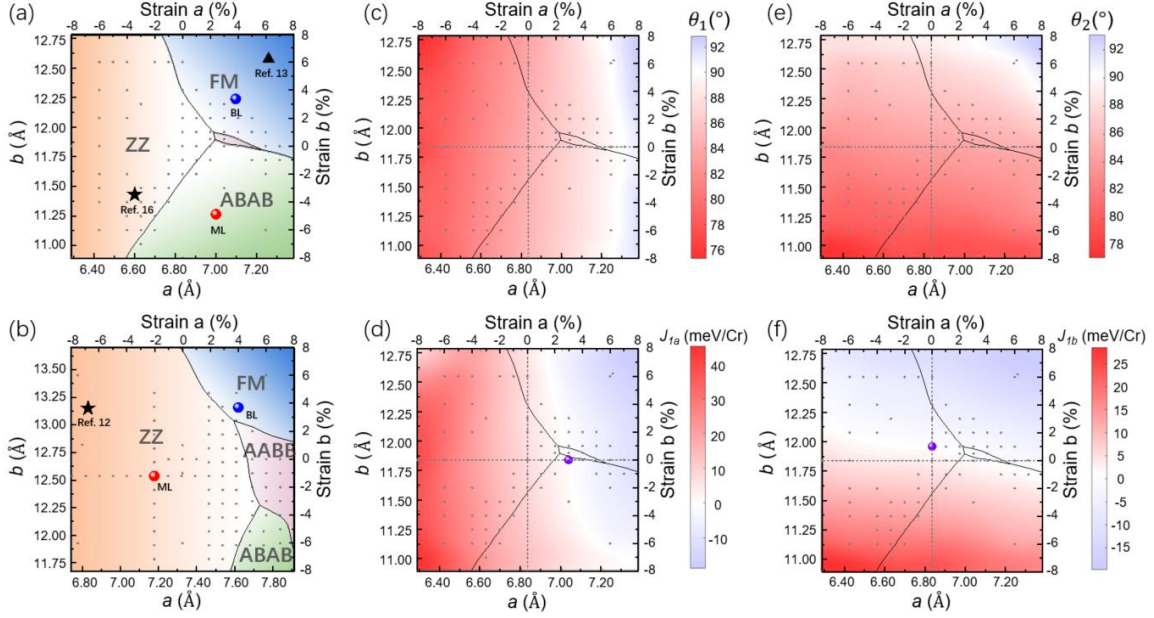


Figure 2. Tunability of intralayer magnetism of monolayer CrSe₂ and CrTe₂. (a) and (b) Phase diagrams of monolayer CrSe₂ (a) and CrTe₂ (b) as a function of lattice constants a and b . Blue, orange, green and purple components represent intralayer FM, ZZ, ABAB and AABB, respectively. Each gray dot represents a theoretical data point that the energies of those four configurations are compared. Red and blue dots label fully relaxed lattice constants under the most energetically favorable magnetic configurations in mono- and bi-layer CrX₂ (X=Se, Te), respectively. Those black triangle and star symbols mark the lattice constants of experimentally synthesized monolayer CrX₂ (X=Se, Te) on different substrates. (c) and (e) θ_1 and θ_2 varying with the lattice constants in monolayer CrSe₂. (d) and (f) Mapping of exchange parameters J_{1a} and J_{1b} as a function of lattice constants. Positive (red) and negative (blue) areas represent AFM and FM spin-exchange coupling, respectively. Phase boundaries of monolayer CrSe₂ are labeled by black lines in (c) - (f).

The FM to ABAB transition shares a similar mechanism under shortening constant b . The shortened b lattice, thus the decreasing θ_2 angle (Fig. 2e), directly flips the sign of J_{1b} at, e.g., $b=11.96$ Å (~ 1.0 % tensile strain) with $a=6.84$ Å (the strain-free constant a value), as marked with the purple dot in Fig. 2f, but has little effect on J_{1a} except with strongly

compressed b values. The flipped sign leads J_{1b} to favor the AFM super-exchange at smaller b values. Thus, the AFM coupling occurs in the b direction, showing the sAFM-ABAB ground-state at the right bottom part of the diagram. Competition between the FM and AFM couplings along b results in a FM-sAFM transition configuration, i.e. sAFM-AABB, appeared in a very small region in-between FM and sAFM-ABAB, in which the two types of magnetic super-exchange occur alternately. In terms of the boundary between ZZ-AFM and sAFM-ABAB, they show competing magnetic couplings in either J_{1a} (AFM versus FM) and J_{1b} (FM versus AFM). They thus roughly bisect the phase diagram outside the FM region.

The phase diagram of monolayer CrTe₂ (Fig. 2b) show a qualitatively similar but quantitatively different pattern to that of the CrSe₂ monolayer. While it is also comprised of those four phases, the ZZ-AFM phase occupies a larger region and the sAFM-AABB phase is more pronounced. A larger tensile strain of $\sim 6.5\%$ to the a direction ($a=7.80$ Å at strain-free constant $b=12.69$ Å) is needed to trigger the positive-to-negative transition of J_{1a} (Fig. S2) while that for J_{1b} of $\sim 1.0\%$ along the b direction ($b=12.81$ Å at strain-free constant $a=7.33$ Å) remains comparable with the value for CrSe₂.

Recently synthesized 2D CrSe₂ and CrTe₂ layers on various substrates and their magnetic characterizations [12, 13, 16] help with verifying the dependence of magnetic orders on lattice constants. In a CrSe₂ monolayer grown on WSe₂ [13], its lattice constant of 3.63 Å ($a = 7.26$ Å and $b = 12.57$ Å, black triangle in Fig. 2a) sits in the FM region of our phase diagram, consistent with the weak FM behavior found in Ref. 9. A smaller lattice constant of 3.3 Å, corresponding to $a=6.6$ Å and $b=11.4$ Å (black star in Fig. 2a), was reported in another CrSe₂ monolayer grown on highly oriented pyrolytic graphite (HOPG). Its lattice constants reside in the ZZ-AFM region, responsible to the absence of ferromagnetic signals in x-ray magnetic circular dichroism (XMCD) measurements [16]. In terms of CrTe₂ monolayers, a sample prepared on a SiC-supporting bilayer graphene substrate shows lattice constants $a = 6.8$ Å and $b = 12.15$ Å (black star in Fig. 2b), locating in the ZZ region of the phase diagram, which was proved using spin-polarized scanning tunneling microscopy (SPSTM) measurements [12].

Interlayer magnetic coupling introduces additional complexity of magnetism in CrX_2 bilayers. Tunability of intralayer magnetism aside, it would be a more interesting and yet to be answered question that whether in-plane strain could tune interlayer magnetism in CrX_2 bi- or few-layers (Fig. 3a). In other words, we are interested if the varying in-plane lattice constants change out-of-plane magnetic coupling in CrX_2 bilayers, which was discussed in details as follows.

Figure 3b shows the phase diagram for the magnetic groundstate of the CrSe_2 bilayer over in-plane lattice constants a and b . It is qualitatively comparable with that of the CrSe_2 monolayer in terms of intra-layer magnetism. Intralayer FM and interlayer AFM, (FM-AFM, $a=7.10 \text{ \AA}$ and $b=12.29 \text{ \AA}$, see Fig. 3a) was used as the strain-free groundstate and thus the reference to calculate exact strain values in the CrSe_2 bilayer, different from that use for the monolayer (see Table S2 for more details). The easy axis in the bilayer only rotates 10° towards the z axis from that of monolayer. Equilibrium in-plane lattice constants of the CrSe_2 bilayer exhibit substantially enlarged in-plane lattice constants (blue dot in Fig. 3b) in comparison with that of the monolayer, as theoretically revealed in CrS_2 [17], CrSe_2 [13, 14] and CrTe_2 [12, 14] bilayers. It thus leads to the FM groundstate for the in-plane magnetism in the CrSe_2 bilayer.

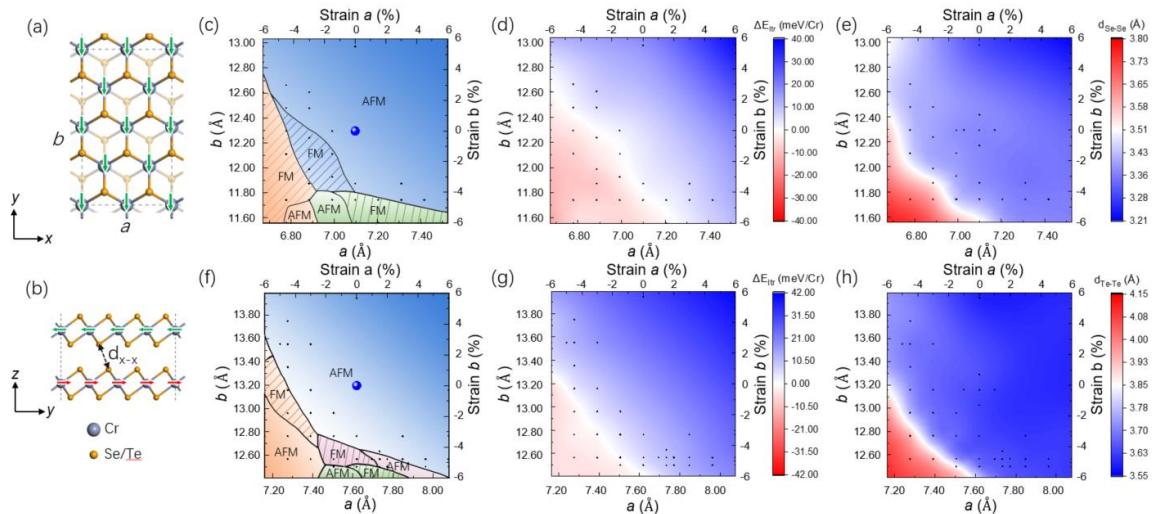


Figure 3. Tunability of intra- and inter-layer magnetisms of CrSe_2 and CrTe_2 bilayers. (a) and (b) Top and side views and magnetic ground state of an AA stacked CrX_2 bilayer. Grey and orange balls represent Cr and Se (Te) atoms, respectively. Lattice constants a and b are denoted in (a). Interlayer Se-

Se (Te-Te) distance is labeled by the black dash arrows in (b). Colored solid arrows on Cr represent the majority spin of up (red) and down (green). (c) Phase diagram of the CrSe₂ bilayer as a function of lattice constants a and b . While the color scheme and presentation style of data points are as the same as that used for the diagrams of monolayers, those shadowed and plain colored regions indicate interlayer magnetic couplings are FM and AFM, respectively. Panel (d) plots the energy difference between interlayer FM and AFM states of the intra-layer FM configuration at different lattice constants. The blue (positive) region represents favored interlayer AFM state and FM for the red (negative) region. (e) Map of the interlayer Se-Se distance with respect to different a and b constants. Panels (f) to (h) duplicate panels (c) to (e) for the CrTe₂ bilayer case.

The interlayer magnetism in the bi- and thicker-layers shows fruitful tunability under in-plane strain. As shown in the phase diagram (Fig. 3c), each colored region (intra-layer magnetism), splits into two sub-regions denoting inter-layer FM (shadowed color) and AFM (plain color) configurations, respectively. The interlayer AFM-FM transition follows two rules depending on the intra-layer magnetism. The inter-layer AFM is more favored with larger in-plane lattice constants in the case of the intra-layer FM configuration. For example, the FM-AFM state of CrSe₂ undergoes an inter-layer magnetic transition to the FM-FM state under a 2.8% compressive strain applied in the a direction. Here, we defined the energy difference between the FM-FM and FM-AFM states as ΔE_{ltr} and plotted its values for CrSe₂ in Fig. 3d where it shows strong in-plane strain dependence. The AFM interlayer exchange (positive ΔE_{ltr}) is gradually suppressed by applying compressive strain to the either lattice. Here, we define the negative of ratio of the interlayer strain to the uniaxial in-plane strain as the interlayer Poisson's ratio. If a finite positive value of it is presented, the shrank in-plane lattice constants should enlarged inter-layer distance d_{X-X} and thus more favor the inter-layer FM coupling, following the Bethe-Slater curve-like (BSC-like) behavior and the super-orbital mediated super-exchange mechanism that we previously revealed in MX₂ bilayers [14].

Figure 3e shows that $d_{\text{Se-Se}}$ could vary from 3.21 to 3.80 Å in the range of $\pm 6\%$ in-plane strain for the CrSe₂ bilayer, which crosses the critical distance of 3.45 Å for the interlayer FM to AFM transition. The interlayer Poisson's ratio is 0.48 (0.46) under the uniaxial strain along the a (b) direction for the CrSe₂ bilayer. Such significant response of the interlayer distance to the in-plane strain ensures the feasibility of tuning out-plane

interlayer magnetic configuration by applying in-plane stress fields. An opposite trend of inter-layer magnetism and in-plane strain was found for the ZZ or ABAB intra-layer magnetism in the CrSe₂ bilayer, termed reversed BSC-like behavior, ascribed to a competition between super-orbital mediated direct- and super-exchanges, which will be elucidated elsewhere.

In terms of the CrTe₂ bilayer, its phase diagram (Fig. 3f) displays a comparable pattern with that of the CrSe₂ bilayer, except the missing FM-FM region and the additional intra-layer AABB configuration. While the interlayer magnetisms of the intra-layer ZZ-AFM and sAFM-ABAB configurations follow the reversed BSC-like behavior, the interlayer spin-exchange interaction in the intra-layer AABB configuration obeys the BSC-like behavior, i.e. interlayer AFM (FM) for larger tensile (compressive or smaller tensile) strains. Another distinct difference of the CrSe₂ and CrTe₂ cases lies in the missing FM-FM region in the CrTe₂ diagram. Energy ΔE_{Itr} of the CrTe₂ bilayer (Fig. 3g) flips its sign in regions where the preferred in-plane magnetism already transforms into ZZ-AFM, sAFM-AABB or sAFM-ABAB. Such delayed sign reversal is ascribed to a much larger transition distance of the CrTe₂ bilayer. Under the $\pm 6\%$ in-plane strain, interlayer distance $d_{\text{Te-Te}}$ of the CrTe₂ bilayer varies from 3.55 to 4.15 Å under, and the interlayer Poisson's ratio is around 0.61 (0.23) under the uniaxial strain along the a (b) direction. Such distance range does not include the interlayer FM-AFM transition distance of 4.32 Å, but other in-plane magnetic configurations emerge before the interlayer AFM-FM transition occurs.

The phase diagrams imply that inter- and intra-layer magnetic orders could be tuned by in-plane strain engineering, which usually utilizes using slightly lattice-mismatched vdW substrates, namely the epitaxy strain. We thus considered an example, i.e. CrTe₂/bilayer graphene (BLG), to see how in-plane epitaxy strain behaves in determining its magnetism. Figure 4a depicts a schematic model of a $10 \times 3\sqrt{3}$ CrTe₂/ $16 \times 4\sqrt{3}$ BLG superlattice, as experimentally determined in a previous work [12]. While the graphene-CrTe₂ stacking order varies from site to site within a domain (red hexagons), no apparent charge transfer and interlayer wavefunction overlap [12-14, 17] were observed between the CrTe₂ layer and the graphene substrate (Fig. 4b). The in-plane epitaxy strain effect thus plays a dominant role in tuning the magnetism of the epitaxial layer. In this particular case,

the nearest Cr-Cr distances are 3.42 and 3.70 ± 0.02 Å in the a and b directions (Fig. 4c left), respectively, which are within the ZZ region of the phase diagram and far from the phase boundaries (see black star in Fig.2b), consistent with the robust ZZ AFM state as depicted in Fig. 4c right.

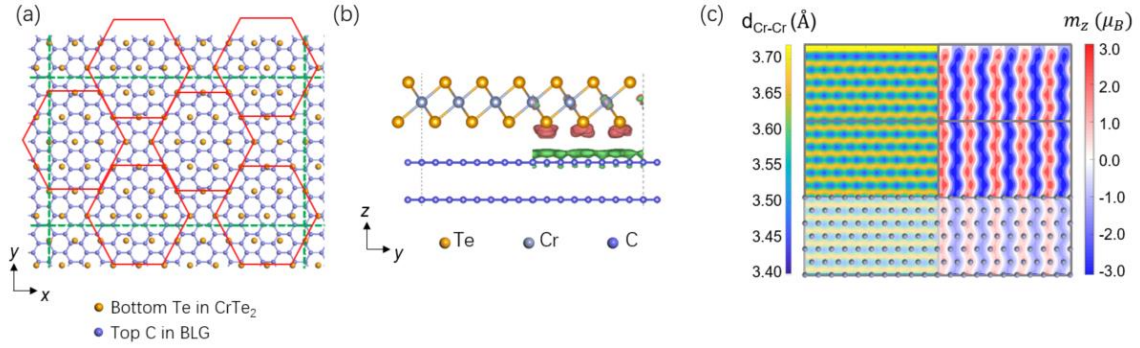


Figure 4. Structure and magnetism of the epitaxial CrTe_2 monolayer on bi-layer graphene. (a) Schematic model of a $10 \times 3\sqrt{3}$ $\text{CrTe}_2/16 \times 4\sqrt{3}$ bilayer graphene (BLG) heterojunction. (b) Side view of the interlayer differential charge density contour of the heterojunction with an isosurface level of $2.0 \times 10^{-4} e/\text{Bohr}^3$. Red and green contours represent charge accumulation and depletion, respectively. (c) Mapping of the nearest Cr-Cr distance (left panel) and magnetic moments (right panel) of Cr atoms in the heterojunction.

In summary, we revealed that the in-plane epitaxy strain is capable of tuning both in-plane (intralayer) and out-of-plane (interlayer) magnetisms in epitaxy CrSe_2 and CrTe_2 mono- and bi-layers. In terms of intra-layer magnetism, the in-plane strain primarily changes the Cr-Se-Cr and Cr-Te-Cr angles that govern the intra-layer spin-exchange couplings, giving rise to the ZZ, ABAB and FM magnetic configurations. Our predicted phase diagrams of monolayers were confirmed with experimentally synthesized 2D CrSe_2 or CrTe_2 samples. A more striking effect lies in that the in-plane strain, through a finite Poisson's ratio, varies the inter-layer distance, which subsequently determines the inter-layer magnetism following a Bethe-Slater curve (BSC) like or a reversed BSC-like behavior depending on the in-plane magnetism. This exceptional effect enables of tuning out-of-plane magnetism using an in-plane strain field. Upon epitaxy of those 2D magnets on a graphene substrate, epitaxy strain still dominantly determines their magnetism because of suppressed interlayer charge transfer. Our calculation suggests a considerable magneto-

elastic effect in 2D CrSe₂ and CrTe₂, and indicate that magnetisms of them can be manipulated in vdW epitaxy by in-plane strain from appropriately selected vdW substrates.

Method

DFT calculations are carried out using the generalized gradient approximation for the exchange-correlation potential, the projector augmented wave method [18] and a plane-wave basis set as implemented in the Vienna ab-initio simulation package (VASP) [19]. A $2 \times 2\sqrt{3}$ supercell of monolayer and bilayer CrX₂ is adopted to take consider of four intralayer magnetic configurations listed in Fig. 1(b)-(e) and a $10 \times 6 \times 1$ k-mesh was used to sample the first Brillouin zone of it. A sufficiently large vacuum layer over 16 Å along the out-of-plane direction was adopted to eliminate the interaction among layers. The kinetic energy cut-off for the plane-wave basis was set to 700 eV for the geometric properties and 600 eV for electronic structure and energy calculations. Dispersion corrections were made at the van der Waals density functional (vdW-DF) level [20], with the optB86b functional for the exchange potential (optB86b-vdW) [21], which was proved to be accurate in describing the structural properties of layered materials [22-24] and was adopted for structure optimization. The shape and volume of mono- and bi-layer structures were fully relaxed until the residual force per atom was less than 0.002 eV/Å. A second-order Methfessel-Paxton smearing method with a sigma value of 0.01 eV was adopted during calculations. For energy comparisons among different magnetic configurations, we used the Perdew–Burke–Ernzerhof (PBE) functional [25] based on the vdW-DF-revealed structures. In-plane strain was defined as $\varepsilon = \frac{a-a_0}{a_0} \times 100\%$, where a_0 and a denote lattice constants before and after applying in-plane strain. From the lattice constants of intralayer FM structure, which maintains the C3 symmetry, $\pm 8\%$ ($\pm 6\%$) strain was considered in both directions and one date point for each 1% (1.5%) strain variation was collected to calculate the phase diagrams of monolayers (bilayers). Besides, 0.5% strain for each point around phase transformation points is adopted to get phase boundaries. The interlayer Poisson's ratio is defined as $\nu_{\perp} = \frac{\Delta h/h}{\varepsilon_{11} + \varepsilon_{22}}$, where ε_{11} and ε_{22} is the in-plane strains along the a and b directions, and h is the interlayer vertical Se-Se (Te-Te) distance (Fig. S5). To approximately estimate the interlayer Poisson's ratio, we made a linear fit on the variations

of interlayer distances under a series of uniaxial strains in directions a or b in a range of $\pm 1.5\%$ with a 0.5% step size (see Fig. S5 for more details). To account for on-site Coulomb interaction to the Cr d orbitals, U and J values of 4.5 eV (3.0 eV) and 0.6 eV, revealed by a linear response method [26] and by comparison with the results of HSE06 [27] in previous work [14], are adopted in CrSe₂ (CrTe₂).

Acknowledgements

We gratefully acknowledge financial support from the Ministry of Science and Technology (MOST) of China (Grant No. 2018YFE0202700), the National Natural Science Foundation of China (Grants No. 61761166009, No. 11974422 and No. 12104504), and the Strategic Priority Research Program of Chinese Academy of Sciences (Grant No. XDB30000000). C.W. was supported by the China Postdoctoral Science Foundation (2021M693479). L.W. was supported by the Outstanding Innovative Talents Cultivation Funded Programs 2021 of Renmin University of China. Calculations were performed at the Physics Lab of High-Performance Computing of Renmin University of China, Shanghai Supercomputer Center.

Reference

- [1] T. Li, S. Jiang, N. Sivadas, Z. Wang, Y. Xu, D. Weber, J.E. Goldberger, K. Watanabe, T. Taniguchi, C.J. Fennie, K. Fai Mak, J. Shan, Pressure-controlled interlayer magnetism in atomically thin CrI_3 , *Nat Mater*, 18 (2019) 1303-1308.
- [2] T. Song, Z. Fei, M. Yankowitz, Z. Lin, Q. Jiang, K. Hwangbo, Q. Zhang, B. Sun, T. Taniguchi, K. Watanabe, M.A. McGuire, D. Graf, T. Cao, J.H. Chu, D.H. Cobden, C.R. Dean, D. Xiao, X. Xu, Switching 2D magnetic states via pressure tuning of layer stacking, *Nat Mater*, 18 (2019) 1298-1302.
- [3] Z. Lin, M. Lohmann, Z.A. Ali, C. Tang, J. Li, W. Xing, J. Zhong, S. Jia, W. Han, S. Coh, W. Beyermann, J. Shi, Pressure-induced spin reorientation transition in layered ferromagnetic insulator $\text{Cr}_2\text{Ge}_2\text{Te}_6$, *Physical Review Materials*, 2 (2018).
- [4] Y. Wang, C. Wang, S.J. Liang, Z. Ma, K. Xu, X. Liu, L. Zhang, A.S. Admasu, S.W. Cheong, L. Wang, M. Chen, Z. Liu, B. Cheng, W. Ji, F. Miao, Strain-Sensitive Magnetization Reversal of a van der Waals Magnet, *Adv Mater*, 32 (2020) e2004533.
- [5] H.Y. Lv, W.J. Lu, D.F. Shao, Y. Liu, Y.P. Sun, Strain-controlled switch between ferromagnetism and antiferromagnetism in 1T-CrX_2 ($\text{X}=\text{Se}, \text{Te}$) monolayers, *Physical Review B*, 92 (2015).
- [6] B.A. Joyce, Molecular beam epitaxy, *Reports on Progress in Physics*, 48 (1985) 1637-1697.
- [7] S.C. Jain, M. Willander, J. Narayan, R.V. Overstraeten, III-nitrides: Growth, characterization, and properties, *Journal of Applied Physics*, 87 (2000) 965-1006.
- [8] R. Ramesh, N.A. Spaldin, Multiferroics: progress and prospects in thin films, *NATURE MATERIALS*, 6 (2007) 21-29.
- [9] A. Koma, K. Sunouchi, T. Miyajima, Fabrication of ultrathin heterostructures with van der Waals epitaxy, *Journal of Vacuum Science & Technology B*, 3 (1985) 724-724.
- [10] A. Koma, Van der Waals epitaxy—a new epitaxial growth method for a highly lattice-mismatched system, *Thin Solid Films*, 216 (1992) 72-76.
- [11] X. Zhang, Q. Lu, W. Liu, W. Niu, J. Sun, J. Cook, M. Vaninger, P.F. Miceli, D.J. Singh, S.W. Lian, T.R. Chang, X. He, J. Du, L. He, R. Zhang, G. Bian, Y. Xu, Room-temperature intrinsic ferromagnetism in epitaxial CrTe_2 ultrathin films, *Nat Commun*, 12 (2021) 2492.
- [12] J.J. Xian, C. Wang, J.H. Nie, R. Li, M. Han, J. Lin, W.H. Zhang, Z.Y. Liu, Z.M. Zhang, M.P. Miao, Y. Yi, S. Wu, X. Chen, J. Han, Z. Xia, W. Ji, Y.S. Fu, Spin mapping of intralayer antiferromagnetism and field-induced spin reorientation in monolayer CrTe_2 , *Nat Commun*, 13 (2022) 257.
- [13] B. Li, Z. Wan, C. Wang, P. Chen, B. Huang, X. Cheng, Q. Qian, J. Li, Z. Zhang, G. Sun, B. Zhao, H. Ma, R. Wu, Z. Wei, Y. Liu, L. Liao, Y. Ye, Y. Huang, X. Xu, X. Duan, W. Ji, X. Duan, Van der Waals epitaxial growth of air-stable CrSe_2 nanosheets with thickness-tunable magnetic order, *Nat Mater*, 20 (2021) 818-825.
- [14] C. Wang, X. Zhou, L. Zhou, Y. Pan, Z.-Y. Lu, X. Wan, X. Wang, W. Ji, Bethe-Slater-curve-like behavior and interlayer spin-exchange coupling mechanisms in two-dimensional magnetic bilayers, *Physical Review B*, 102 (2020).
- [15] W. Geertsma, D. Khomskii, Influence of side groups on 90 degrees superexchange: A modification of the Goodenough-Kanamori-Anderson rules, *Phys Rev B Condens Matter*, 54 (1996) 3011-3014.
- [16] M. Liu, Y.L. Huang, J. Gou, Q. Liang, R. Chua, Arramel, S. Duan, L. Zhang, L. Cai, X. Yu, D. Zhong, W. Zhang, A.T.S. Wee, Diverse Structures and Magnetic Properties in Nonlayered Monolayer Chromium Selenide, *J Phys Chem Lett*, 12 (2021) 7752-7760.
- [17] C. Wang, X. Zhou, Y. Pan, J. Qiao, X. Kong, C.-C. Kaun, W. Ji, Layer and doping tunable ferromagnetic order in two-dimensional CrS_2 layers, *Physical Review B*, 97 (2018).
- [18] P.E. Blöchl, Projector augmented-wave method, *Physical Review B*, 50 (1994) 17953-17979.

- [19] G. Kresse, J. Furthmüller, Efficient iterative schemes for ab initio total-energy calculations using a plane-wave basis set, *Physical Review B*, 54 (1996) 11169-11186.
- [20] M. Dion, H. Rydberg, E. Schröder, D.C. Langreth, B.I. Lundqvist, Van der Waals Density Functional for General Geometries, *Physical Review Letters*, 92 (2004) 246401.
- [21] J. Klimeš, D.R. Bowler, A. Michaelides, Van der Waals density functionals applied to solids, *Physical Review B*, 83 (2011) 195131.
- [22] J. Hong, Z. Hu, M. Probert, K. Li, D. Lv, X. Yang, L. Gu, N. Mao, Q. Feng, L. Xie, J. Zhang, D. Wu, Z. Zhang, C. Jin, W. Ji, X. Zhang, J. Yuan, Z. Zhang, Exploring atomic defects in molybdenum disulphide monolayers, *Nat Commun*, 6 (2015) 6293.
- [23] J. Qiao, Y. Pan, F. Yang, C. Wang, Y. Chai, W. Ji, Few-layer Tellurium: one-dimensional-like layered elementary semiconductor with striking physical properties, *Science Bulletin*, 63 (2018) 159-168.
- [24] Y. Zhao, J. Qiao, Z. Yu, P. Yu, K. Xu, S.P. Lau, W. Zhou, Z. Liu, X. Wang, W. Ji, Y. Chai, High-Electron-Mobility and Air-Stable 2D Layered PtSe₂ FETs, *Adv Mater*, 29 (2017).
- [25] J.P. Perdew, K. Burke, M. Ernzerhof, Generalized Gradient Approximation Made Simple, *Phys Rev Lett*, 77 (1996) 3865-3868.
- [26] M. Cococcioni, S. de Gironcoli, Linear response approach to the calculation of the effective interaction parameters in the LDA+U method, *Physical Review B*, 71 (2005).
- [27] J. Heyd, G.E. Scuseria, M. Ernzerhof, Hybrid functionals based on a screened Coulomb potential, *The Journal of Chemical Physics*, 118 (2003) 8207-8215.

Supplemental Information

In-plane epitaxy strain tuning intralayer and interlayer magnetic couplings in CrSe₂ and CrTe₂ mono- and bi-layers

Linlu Wu^{1, †}, Linwei Zhou^{1, †}, Xieyu Zhou¹, Cong Wang^{1, *} and Wei Ji^{1, *}

¹*Beijing Key Laboratory of Optoelectronic Functional Materials & Micro-Nano Devices,
Department of Physics, Renmin University of China, Beijing 100872, P.R. China*

Corresponding authors: C.W. (email: wcp@ruc.edu.cn), W.J. (email: wji@ruc.edu.cn)

† These authors contributed equally to this work.

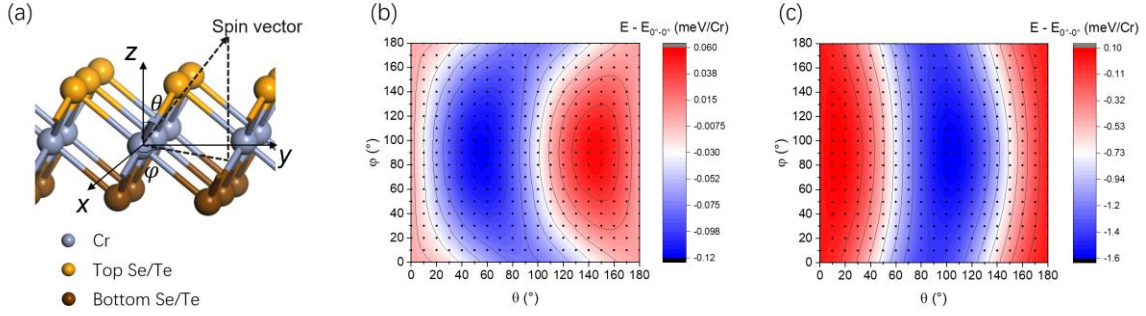


Figure S1. Calculation of magnetic anisotropy energy (MAE) and easy axes of monolayer CrSe₂ and CrTe₂. (a) Schematic model of monolayer CrX₂. The grey, orange and brown balls represent Cr, top-Se (Te) and bottom-Se (Te), respectively. Directions x , y , and z correspond to those three lattice vectors and are perpendicular to each other. Angles θ and φ are defined to describe directions of spin vectors. (b) and (c) Calculation of MAE of monolayer CrSe₂ and CrTe₂, respectively. Relative total energies with magnetization directions fixed in different directions (with respect to $E_{0^\circ-0^\circ}$, which denotes the energy with magnetization directions fixed in the z direction). Easy axes are in the y - z plane and are 60° and 100° off the z axis in CrSe₂ and CrTe₂, respectively.

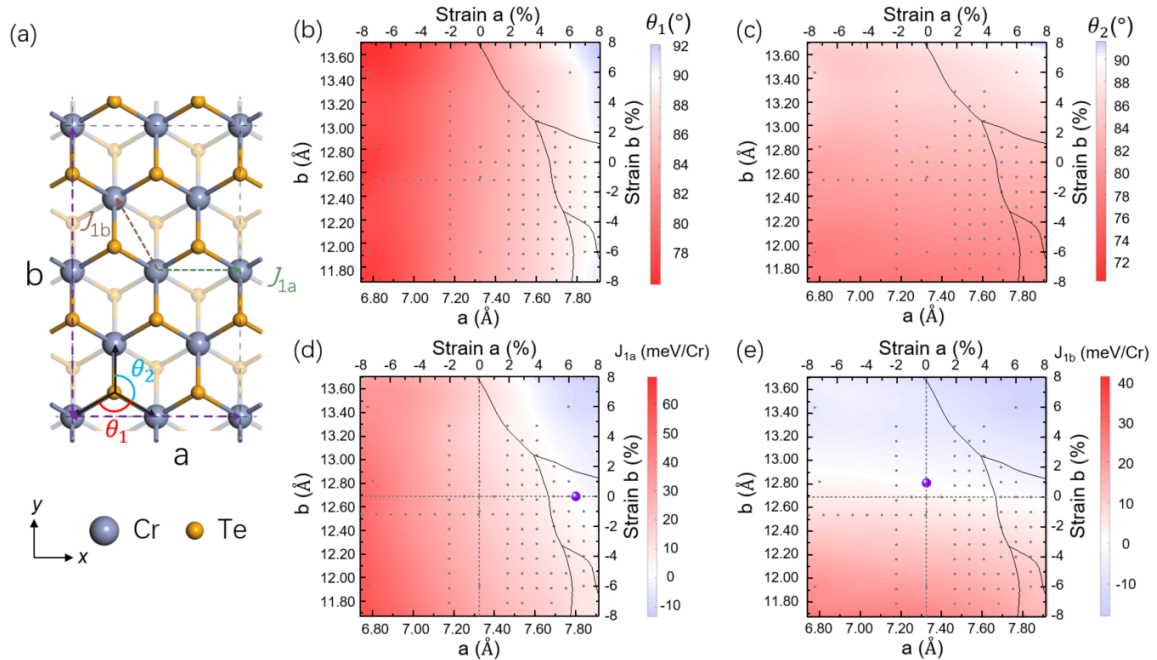


Figure S2. Variations of Cr-Te-Cr angles and exchange parameters with lattice constants in monolayer CrTe₂. (a) Top view of a $2 \times 2\sqrt{3}$ supercell of monolayer CrTe₂. Lattice constants a and b are labeled by purple dash lines. The Cr-Te-Cr angles θ_1 and θ_2 are labeled by arcs. Exchange parameters J_{1a} and J_{1b} are labeled by green and brown dash lines, respectively. (b) and (c) θ_1 and θ_2 vary with lattice constants in monolayer CrTe₂. (d) and (e) Mapping of exchange parameter J_{1a} and J_{1b}

as a function of lattice constants. Positive (red) region and negative (blue) region represent AFM and FM exchange, respectively. Phase boundaries of monolayer CrTe_2 are labeled by black lines in (b) - (e).

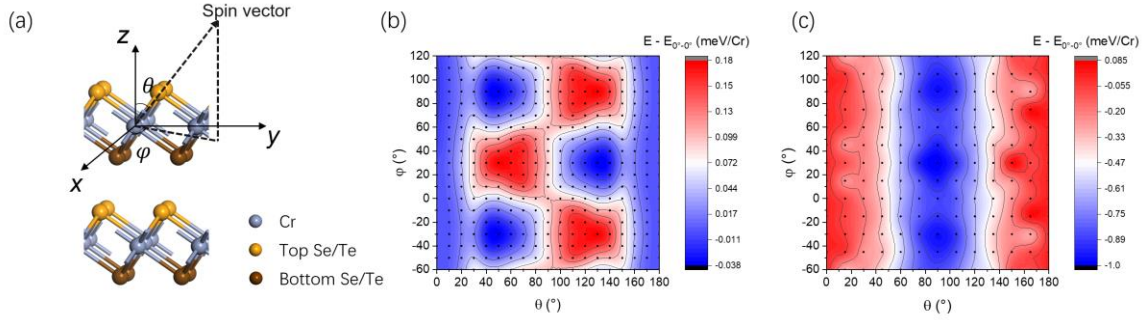


Figure S3. Calculation of magnetic anisotropy energy (MAE) and easy axes of bilayer CrSe_2 and CrTe_2 . (a) Schematic model of bilayer CrX_2 ($X=\text{Se}, \text{Te}$). The grey, orange and brown balls represent Cr, top-Se (Te) and bottom-Se (Te) in each layer, respectively. Directions x , y , and z correspond to those three lattice vectors and are perpendicular to each other. Angles θ and φ are defined to describe directions of spin vectors. (b) and (c) Calculation of MAE of bilayer CrSe_2 and CrTe_2 , respectively. Relative total energies with magnetization directions fixed in different directions (with respect to $E_{0^\circ-0^\circ}$, which denotes the energy with magnetization directions fixed in the z direction). Easy axis of bilayer CrSe_2 is in the y - z plane and 50° off the z axis, while in bilayer CrTe_2 it is along the y axis.

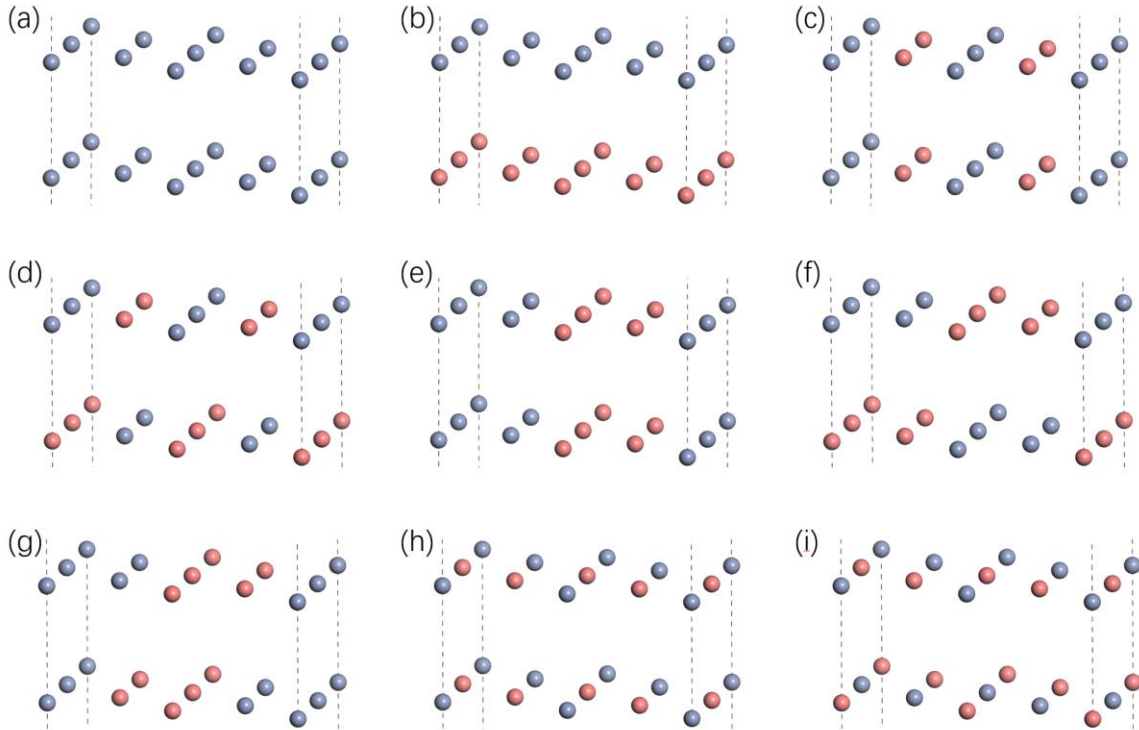


Figure S4. Schematic representation of nine magnetic orders considered in bilayer CrSe_2 and CrTe_2 . The gray and pink balls represent the magnetic moment up and down on Cr atoms, respectively. (a) FM-FM; (b) FM-AFM; (c) ABAB-FM; (d) ABAB-AFM; (e) AABF-FM; (f) AABF-AFM1; (g) AABF-AFM2; (h) AABF-AFM3; (i) AABF-AFM4.

AABB-AFM2; (h) ZZ-FM; (i) ZZ-AFM. The first and second labels represent intralayer and interlayer magnetism, respectively.

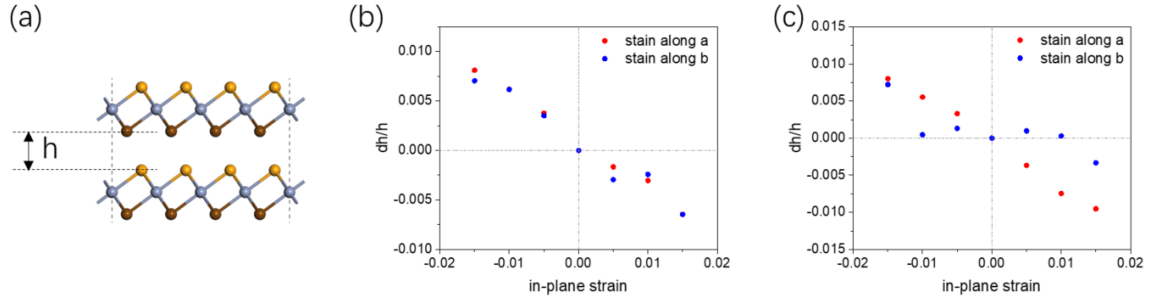


Figure S5. Calculation of interlayer Poisson's ratio in bilayer CrSe₂ and CrTe₂. The interlayer Poisson's ratio is defined as $\nu_{\perp} = \frac{\Delta h/h}{\varepsilon_{11} + \varepsilon_{22}}$, where ε_{11} and ε_{22} is the in-plane strains along the a and b directions, and h is the interlayer vertical Se-Se (Te-Te) distance. (a) Side view of bilayer CrSe₂ (CrTe₂) and definition of interlayer vertical distance. (b) and (c) Variations of $\Delta h/h$ on uniaxial strain along the a (b) in bilayer CrSe₂ and CrTe₂, respectively.

Table S1. Geometric and magnetic details of monolayer CrSe₂ and CrTe₂. Four magnetic configurations are labeled in Fig 1(b)-(d). 'Mag. Config.' is the abbreviation of magnetic configuration. ΔE is the energy difference from the ground state. Nearest Cr-Cr distances are listed in the table. θ_1 , θ_2 and θ_3 are labeled in Fig. 1a. Structures are optimized with optB86b-vdW+UJ, and all energy and magnetic moment related values are calculated using PBE+UJ.

Fully relaxed	Intralayer Mag. Config.	ΔE (meV/Cr)	a (Å)	b (Å)	Cr-Cr distance (Å)			Angle of Cr-X-Cr (°)			Mag. Mom. (μB)	
					r_1	r_2	r_3	θ_1	θ_2	θ_3	Cr	Se
ML-CrSe ₂	FM	22.40	6.84	11.84	3.42	3.42	3.42	84.6	84.6	84.6	3.09	-0.21
	sAFM-ABAB	0.00	7.00	11.26	3.50	3.32	3.32	86.8	81.7	81.7	3.02	0.04
	sAFM-AABB	10.08	6.96	11.43	3.48	3.38	3.38	86.0	83.4	83.4	3.12	0.18/0.06
	ZZ	2.97	6.75	11.68	3.38	3.42	3.34	83.4	82.3	84.5	3.03	0.03
ML-CrTe ₂	FM	39.57	7.33	12.66	3.66	3.66	3.66	84.3	84.1	84.1	3.06	-0.18
	sAFM-ABAB	3.25	7.52	11.98	3.76	3.54	3.54	86.5	80.8	80.8	3.02	0.04
	sAFM-AABB	5.49	7.50	12.12	3.75	3.63	3.63	86.0	83.1	83.1	3.14	0.16/0.06
	ZZ	0.00	7.18	12.54	3.59	3.66	3.57	82.1	81.7	83.9	3.06	0.04

Table S2. Energy comparison of nine magnetic configurations in bilayer CrSe₂ and CrTe₂. Structures are optimized with optB86b-vdW+UJ. In-plane FM is kept in structure optimization. Whether interlayer AFM or FM are adopted in structure optimization, the energetically favored magnetism is always FM-AFM (intralayer FM and interlayer AFM). Each row in the table lists relative energy of nine magnetic orders with FM-AFM.

Unit (meV/Cr)	Fully relaxed structure	Mag. Config.								
		FM-FM	FM-AFM	ABAB-FM	ABAB-AFM	AABB-FM	AABB-AFM1	AABB-AFM2	ZZ-FM	ZZ-AFM
BL-CrSe ₂	FM-AFM	2.42	0.00	31.42	33.73	21.41	28.21	26.71	31.39	32.76
	FM-FM	1.21	0.00	31.27	33.49	20.69	27.54	25.71	28.22	29.77
BL-CrTe ₂	FM-AFM	7.47	0.00	40.21	43.38	22.53	29.11	22.24	36.44	36.65
	FM-FM	6.64	0.00	38.34	41.45	21.29	27.67	21.08	34.02	34.49

Table S3. Geometric and magnetic details of bilayer CrSe₂ and CrTe₂. ‘Mag. Config.’ is the abbreviation of magnetic configuration. Lattice constants ‘*a*’ and ‘*b*’ are labeled in Fig. 3a. ‘*r*’ denotes the nearest Cr-Cr distance. Layer height is the vertical distance between the top and bottom Se (Te) sublayer in a Se-Cr-Se (Te-Cr-Te) layer. Interlayer Cr-Cr distance and Se-Se (Te-Te) distance (labeled in Fig.3a) are also listed in the table. ΔE is the energy difference from the ground state.

	Mag. Config.	<i>a</i> (Å)	<i>b</i> (Å)	<i>r</i> (Å)	layer height (Å)	interlayer Cr-Cr (Å)	interlayer X-X (Å)	ΔE (meV/Cr)	mag Cr (μB)	mag Se (μB)
BL-CrSe ₂	FM-AFM	7.10	12.29	3.55	3.00	5.67	3.37	0.00	3.14	0.21
	FM-FM	7.06	12.23	3.53	3.01	5.71	3.39	2.40	3.10	-0.20
BL-CrTe ₂	FM-AFM	7.62	13.20	3.81	3.22	6.11	3.64	0.00	3.14	0.18
	FM-FM	7.60	13.17	3.80	3.22	6.15	3.66	7.47	3.09	-0.17